Rare Metal Materials and Engineering
Volume 52, Issue 5, May 2023
Available online at www.rmme.ac.cn

Science Press

Cite this article as: Zhang Peng, Zhao Xinsheng, Rao Sixian. Effects of Artificial Aging and Corrosion Medium Concentration on Electrochemical Corrosion Behavior of 2A97 Al-Cu-Li Alloys[J]. Rare Metal Materials and Engineering, 2023, 52(05): 1573-1582.

ARTICLE

Effects of Artificial Aging and Corrosion Medium Concentration on Electrochemical Corrosion Behavior of 2A97 Al-Cu-Li Alloys

Zhang Peng, Zhao Xinsheng, Rao Sixian

School of Mechanical Engineering, Anhui University of Technology, Ma'anshan 243032, China

Abstract: The corrosion resistance of 2A97-T3 and 2A97-T6 Al-Cu-Li alloys was studied by the electrochemical method through potentiodynamic polarization curves. The typical third generation 2060-T8, 2099-T83, and 2024-T4 alloys were used as reference for comparison. Through the analysis of electrochemical parameters and corrosion morphology, the results reveal that the corrosion resistance of the alloys in NaCl solution of different concentrations is as follows: 2A97-T3>2A97-T6>2024-T4>2060-T8>2099-T83. With increasing the concentration of NaCl solution, the corrosion potential (E_{Corr}) of all alloys is decreased. Moreover, the surface pitting and intergranular corrosion become severe. The T_1 phase greatly increases with more uniform distribution in 2A97-T6 alloy, which is obtained from the 2A97-T3 alloy after the solid solution coupled with double-stage artificial aging treatment. Consequently, the heat treatment process reduces the corrosion potential of 2A97-T6 Al alloy, which leads to the slightly weaker corrosion resistance of 2A97-T6 Al alloy than that of 2A97-T3 alloy. The disintegration of the intergranular θ phase induces the exfoliation corrosion morphology of 2A97-T3 alloy, and the pitting morphology of 2A97-T6 alloy is caused by the dissolution of intragranular T_1 phase.

Key words: Al-Cu-Li alloy; electrochemical polarization; corrosion potential; heat treatment; corrosion morphology

Al-Cu-Li alloys become promising lightweight aerospace structural materials in recent years due to their low density, high elastic modulus, high specific strength, and specific stiffness[1–5]. The traditional 2XXX and 7XXX high-strength aluminum alloys are gradually replaced by the third-generation Al-Cu-Li alloys[6–9]. 2A97 alloy is a third-generation Al-Cu-Li alloy, which has superior performance of high strength, good weldability, and high damage resistance. Therefore, the 2A97 alloy is commonly applied to aircraft structural parts nowadays, such as the fuselage skin, fairing, air intake lip, and fuel tank[10–13]. The corrosion resistance of 2A97 alloy is of great significance for the long-term service in corrosive environment.

Some scholars investigated the effect of precipitation on the mechanical properties of 2A97 alloy after different heat treatments, including elongation, tensile strength, and fatigue strength[14–18]. The corrosion resistance of 2A97 Al-Cu-Li alloy is affected by the type, quantity, and distribution of the precipitated phase, and the precipitated phase is controlled by the heat treatment process. Zhang et al[19] discussed the effect of precipitate distribution on the corrosion behavior of 2A97-T6 alloy in 3.5wt% NaCl solution, and found that the localized plastic strain is introduced to the alloy during sheet fabrication. As a result, the dense T_1 phase precipitate bands and precipitate-free bands both appear in the selected grains. The T_1 phase in the dense precipitation bands is prone to dissolution, which contributes to the intragranular corrosion in the alloy, presenting the corrosion bands. Luo et al[20] investigated the corrosion behavior of 2A97-T6 alloy in NaCl solution. The uneven distribution of orientation in 2A97 alloy leads to the relatively high storage energy of some grains. During the development of crystal pitting, these grains are preferentially attacked as local anodes. Chen et al[21] studied the corrosion behavior of 2099 Al-Li alloy in NaCl solution of different concentrations, and found that 2099 Al-Li alloy has fine corrosion resistance against the NaCl solution. The

Received date: October 19, 2022
Foundation item: Key Projects of Scientific Research in Colleges and Universities of Anhui Provincial Department of Education (KJ2021A036); Major Natural Science Research Project of Anhui Provincial Department of Education (KJ2016SD09)
Corresponding author: Zhang Peng, Ph. D., Lecturer, School of Mechanical Engineering, Anhui University of Technology, Ma'anshan 243032, P. R. China, E-mail: zhangpeng_105@ahut.edu.cn

corrosion rate is increased with increasing the chloride ion concentration, and the main form of corrosion failure is pitting.

The precipitated phases in Al-Cu-Li alloy are mainly associated with the heat treatment process. However, the effect mechanism of the precipitated phases on the corrosion behavior, particularly the intergranular corrosion, of Al-Cu-Li alloy requires further research[22–23]. With prolonging the aging duration in a certain extent, the intergranular corrosion sensitivity is gradually increased. With further prolonging the aging duration, the intergranular corrosion sensitivity is decreased and the degree of pitting corrosion is increased. Meanwhile, the aging treatment usually involves the alloy potential change[24–25]. According to Ref.[26], the intergranular grains of Al-Cu-Li alloys result in the pitting of precipitate-free zones at grain boundaries. It is also noted that the width of the precipitate-free zone and the size of the T_1 phase precipitate at grain boundary are directly related to the intergranular corrosion sensitivity of the Al-Cu-Li alloy. Zhang et al[27] reported the corrosion behavior of 2A97-T3 Al-Cu-Li alloy in NaCl solution, and found that the distribution of local T_1 and T_B phases of alloy has an effect on the corrosion behavior. Buchheit et al[28] showed that the selective dissolution of T_1 phase precipitate at grain boundary leads to the intergranular corrosion. Besides, the grain boundaries with high density of T_1 phase precipitate have high susceptibility to intergranular corrosion when the Al-Cu-Li alloys are immersed in NaCl solution. Zhang et al[29] investigated the impact of precipitate distribution on the corrosion behavior of 2A97-T6 Al-Cu-Li alloy in 3.5wt% NaCl solution, and found that the introduction of plastic strain during the rolling process results in the non-uniform distribution of T_1 phase. Additionally, the intragranular corrosion also occurs due to the preferential dissolution of T_1 phase in the thick precipitation zone. Luo et al[30] investigated the localized corrosion behavior of 2A97-T4 Al-Cu-Li alloys in 3.5wt% NaCl solution, and found that the localized corrosion usually starts at the θ phase grains. In addition, the θ phase becomes cathode during the corrosion process, resulting in the anodic dissolution of alloy matrix. Niu et al[31] adopted potentiostatic polarization measurement to compare the corrosion resistance of Al, 2A97 Al-Li alloy, 2024 Al alloy, 6061 Al alloy, and 7050 Al alloy. Results show that 2A97 Al-Li alloy has the optimal corrosion resistance in the initial corrosion stage. In the stable corrosion process, the corrosion resistance of 2A97 alloy is better than that of 2024 Al alloy, 6061 Al alloy, and Al material, but worse than that of 7050 alloy.

Although the corrosion resistance of 2A97 alloy has been researched, its electrochemical corrosion behavior is rarely reported. The electrochemical corrosion mechanism of 2A97 Al-Li alloy after different heat treatments in NaCl solution of different concentrations requires further study. The corrosion resistance of 2A97-T3 and 2A97-T6 alloy was studied by the electrochemical method through potentiodynamic polarization curve analysis. The typical third-generation alloys of 2060-T8 Al-Cu-Li alloy, 2099-T83 Al-Cu-Li alloy, and 2024-T4 Al alloy were used as the reference objects, which are the main structural components of C919 and A380 large aircrafts[1,32]. The corrosion solution was 2wt% , 3.5wt% (simulated seawater), and 5wt% NaCl solution. This research provided a theoretical and practical foundation for the investigation of long-term corrosion resistance of 2A97 Al-Cu-Li alloy.

1 Experiment

The 2A97-T3, 2060-T8, and 2099-T83 Al-Cu-Li alloys and 2024-O Al alloy were the raw materials. The 2A97-T6 Al-Cu-Li alloy was obtained from 2A97-T3 alloy after the solid solution processing (520 °C/1.5 h), quenching, and artificial aging (200 °C/6 h+165 °C/6 h)[10,13]. After 2024-O alloy was heated to 495 °C in the furnace for 35 min, quenched, and naturally aged for 120 h, 2024-T4 Al alloy was obtained. The materials used in this research were provided by Xi'an Aircraft Industry (Group) Co., Ltd. The thickness of all alloy specimens was 1.5 mm. ARL Advant X Intellipower 3600 X-ray fluorescence (XRF) spectrometry was adopted to determine the element content of the alloys, and their chemical composition is shown in Table 1.

The specimen was prepared according to GB/T 24196-2009 standard, and the size was 10 mm×10 mm×1.5 mm. The copper wire was bonded to the specimen through conductive copper foil tape. The epoxy resin was applied for cold mosaic sealing and the working face was exposed. The specimen working face was ground sequentially by 600#, 1000#, 1500#, and 2000# SiC paper in water and then polished. The ethanol was adopted to remove the oil from the specimen surface, and then the deionized water was used to clean the specimen surface. Finally, the specimen was dried by cold air.

The electrochemical test was performed by German Zahner Zennium IM6 electrochemical workstation, as shown in Fig.1. The three-electrode system was employed for the potentiodynamic polarization test, which contained a reference electrode (RE), a counter electrode (CE), and a working electrode (WE). RE was the saturated Calomel electrode (SCE), which was used to accurately control the electrode potential of WE. CE was a platinum sheet, which played an important role in current conduction. The alloys acted as WE, which were used for electrochemical reactions on the electrode surface. The corrosion solution was 2wt% , 3.5wt% , and 5wt% NaCl solution. The potentiodynamic polarization test was performed after the open circuit potential (E_{op}) was stabilized. The scanning was conducted from −1.0 V to 1.0 V with the scanning rate of 1 mV/s. As shown in Fig.2, HIROX-7700 three-dimensional morphology microscope was adopted to observe the surface corrosion and the pitting corrosion morphologies. The deepest pit was observed and characterized of each specimen.

2 Results and Discussion

Fig.3a exhibits the potentiodynamic polarization curves of different alloys in 2wt% NaCl solution, which are all similar

Table 1 Chemical composition of different alloys (wt%)

Alloy	Cu	Li	Zn	Mg	Mn	Zr	Fe	Ag	Si	Ti	Al
2A97	3.55	1.31	0.50	0.37	0.31	0.11	0.044	<0.03	<0.03	0.024	Bal.
2060-T8	3.81	0.8	0.311	0.793	0.269	0.169	0.02	0.527	0.07	0.0281	Bal.
2099-T83	2.22	1.87	0.581	0.352	0.276	0.122	0.023	-	0.048	0.026	Bal.
2024-T4	6.12	-	0.086	1.15	1.24	-	1.17	-	0.16	0.022	Bal.

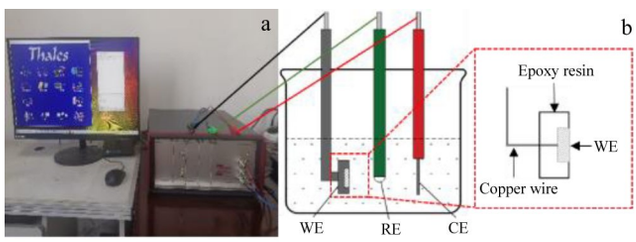

Fig.1 Appearance of Zahner Zennium IM6 electrochemical workstation (a) and schematic diagram of three-electrode system (b)

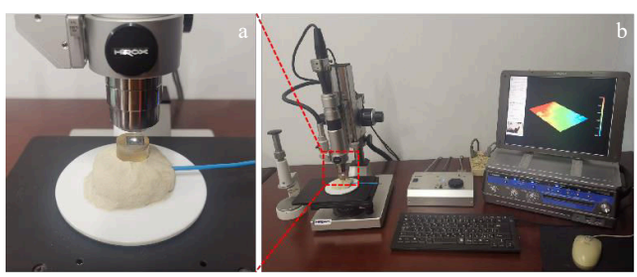

Fig.2 Appearances of HIROX-7700 three-dimensional microscope for surface morphology observation (a) and scanning (b)

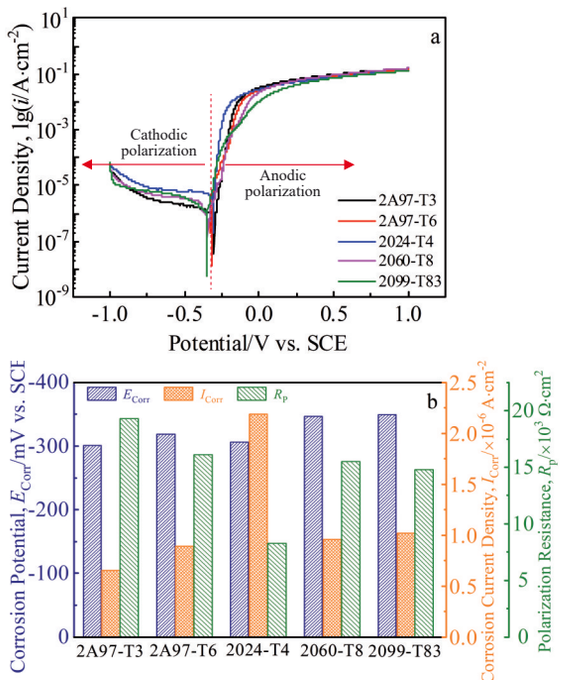

Fig.3 Potentiodynamic polarization curves (a) and electrochemical parameters (b) of different alloys immersed in 2wt% NaCl solution

to each other. No obvious passivation region can be observed. The anodic branch of the polarization curve indicates the typical dissolution behavior of active metals. The corrosion current density (I_{Corr}) increases sharply at the beginning of anodic polarization. The greater the corrosion potential (E_{Corr}), the lower the corrosion sensitivity, and the less the corrosion. The greater the I_{Corr}, the faster the corrosion rate[33–34]. Fig. 3b shows the electrochemical parameter histogram of each alloy. It can be seen that E_{Corr} of different alloys can be arranged in order, as follows: 2A97-T3>2024-T4>2A97-T6>2060-T8> 2099-T83. This result indicates that the spontaneous corrosion reaction of 2A97-T3 alloy is the slightest, i.e., the corrosion reaction can hardly occur in 2A97-T3 alloy. Nevertheless, the E_{Corr} value of 2024-T4 alloy (−306.5 mV) is very close to that of 2A97-T3 alloy (− 301.0 mV), which suggests that the corrosion susceptibility of the 2024-T4 alloy is also very low. The E_{Corr} values of 2060-T8 and 2099-T83 alloys are −346.5 and − 349.5 mV, respectively. Compared with 2060-T8 and 2099-T83 alloys, the 2A97-T6 alloy has the largest E_{Corr} value of − 319.3 mV. The 2099-T83 alloy can easily be corroded among all these alloys. The 2A97-T6 alloy has relatively higher corrosion susceptibility, compared with the 2A97-T3 alloy. The E_{Corr} value of 2A97 alloys is closely related to the evolution of precipitation phase after the heat treatment process. The inconsistent potential is caused by the difference in chemical composition between the secondary phase and the surrounding matrix. The adjacent areas with different potential levels constitute the primary battery and the anodic dissolution occurs in the corrosive medium, which results in the localized corrosion of alloys. The corrosion preferentially occurs in the dense T_1 phase precipitate zone and the alloy is susceptible to intergranular corrosion in the Cl^- environment[35–37]. After the 2A97-T3 alloy is heat-treated by the solid solution processing (520 °C/1.5 h) and double-stage artificial aging (200 ° C/6 h+165 ° C/6 h), the main strengthening precipitates are T_1, θ, and δ' phases. In addition, the T_1 phase increases obviously without significant size change, and its distribution is more uniform[13,38–41]. In the corrosive solution, the T_1 phase acts as the anode and the matrix around T_1 phase acts as the cathode to form the primary battery. Thus, the anodic dissolution of T_1 phase occurs. The T_1 phase reduces the potential difference between grain boundaries and grains, and the uniform corrosion occurs in grains[42–44]. The more the T_1 phase precipitates, the lower the E_{Corr} value, the higher the corrosion sensitivity, and the easier the corrosion initiation.

The corrosion potential E_{Corr} reflects the difficulty of alloy

corrosion from the thermodynamic perspective, and the corrosion rate determines the service life of components. The I_{Corr} and polarization resistance (R_p) are vital parameters to evaluate the corrosion kinetics of alloys. The metal surface area (S) of the whole working electrode can be regarded as the anode area for uniform corrosion, and the current (I) was measured. Thus, $I_{Corr}=I/S$. The metal corrosion is caused by the dissolution of anode alloy and the corrosion rate is proportional to I_{Corr}. The smaller the I_{Corr}, the slower the alloy dissolution, and the better the corrosion resistance. R_p is the resistance to corrosion reaction in the corrosion system. The larger the R_p value, the smaller the corrosion current. Fig. 3b displays that the I_{Corr} value of 2A97-T3 alloy is the smallest of 0.656 μA/cm^2, and its R_p is the largest of 19.3 kΩ. Therefore, the 2A97-T3 alloy has the optimal corrosion resistance based on its low corrosion sensitivity and slow corrosion rate. In addition, the I_{Corr} value (2.19 μA/cm^2) of 2024-T4 alloy is the largest, which demonstrates that the dissolution rate of surface alloy is the largest. Therefore, the corrosion sensitivity of 2024-T4 alloy is low according to its E_{Corr} value, but its corrosion rate is rapid after the corrosion begins. This result indicates that the surface of 2024-T4 alloy is sacrificed to prevent the matrix from corrosion. The I_{Corr} value (0.894 μA/cm^2) of 2A97-T6 alloy is less than that of 2060-T8 (0.96 μA/cm^2) and 2099-T83 (1.02 μA/cm^2) alloys. However, the R_p value (16.1 kΩ·cm^2) of 2A97-T6 alloy is larger than that of 2060-T8 (15.5 kΩ·cm^2) and 2099-T83 (14.8 kΩ·cm^2) alloys. Through the comprehensive analysis of E_{Corr}, I_{Corr}, and R_p, the 2A97-T3 alloy possesses the optimal corrosion resistance in NaCl solution of low concentration (2wt%). The 2A97-T6 alloy has relatively good corrosion resistance, compared with the 2060-T8 and 2099-T83 alloys.

The corrosion resistance can also be evaluated through the surface morphology and 3D morphology analyses. As shown in Fig. 4, the 2A97-T6 alloy surface shows typical pitting morphology with good surface integrity. The surfaces of the other alloys present intergranular corrosion morphologies. According to Ref. [45], the artificial aging treatment can reduce the susceptibility to intergranular corrosion, but it does not necessarily improve the pitting resistance of alloys. The amount of T_1 phase in 2A97-T6 alloy is more than that in 2A97-T3 alloy, which reduces the intragranular potential. The driving force of anodic dissolution of the grain boundary phase is the potential difference between the intragranular and grain boundary phases, which decreases the susceptibility to the intergranular corrosion[35–37,46]. Additionally, the increasing T_1 phase can also lead to the corrosion of matrix grains[46]. Therefore, the 2A97-T6 alloy is prone to pitting corrosion because of grain corrosion. Among these alloys, the pit depth is the smallest of 30.21 μm for the 2024-T4 alloy. The 2024-T4 alloy surface is completely corroded. The external corrosion potential is too high at the initial corrosion stage, which causes the passive film to rapidly rupture. Then, the pitting corrosion becomes severe and extends. Eventually, the surface of the 2024-T4 alloy is gravely corroded[47]. The corrosion morphologies of 2066-T8 and 2099-T83 alloys present obvious localized intergranular corrosion. The pit depth of 2099-T83 alloy is the largest of 47.17 μm. In conclusion, among these alloys, the corrosion resistance of the 2A97-T3 and 2A97-T6 alloys is the best, whereas that of 2099-T83 alloy is the worst.

Fig. 5 exhibits the potentiodynamic polarization curves and electrochemical parameters of different alloys immersed in 3.5wt% NaCl solution. The order of E_{Corr} values of different alloys can be arranged as follows: 2A97-T3>2A97-T6>2024-T4>2060-T8>2099-T83. This result is consistent with that in Fig. 3. Furthermore, the E_{Corr} value of each alloy immersed in 3.5wt% NaCl solution is lower than that immersed in 2wt% NaCl solution. Particularly, the E_{Corr} value of 2A97-T3 alloy decreases from −301.0 mV to −311.5 mV, and the decrement is 10.5 mV. Meanwhile, the E_{Corr} value of 2099-T83 alloy decreases from −349.3 mV to −375.5 mV, and the decrement is 26.2 mV. These phenomena all result from the increase in Cl^- concentrations in the NaCl solution. Consequently, the corrosion potential shifts slightly to the positive direction, leading to more spontaneous corrosion of the alloys and the easier corrosion reactions[48]. The E_{Corr} value of 2A97-T3 alloy does not significantly fluctuate with increasing the NaCl concentration, which indicates that the corrosion sensitivity of 2A97-T3 alloy is still the lowest.

When the NaCl solution concentration increases from 2wt% to 3.5wt%, the Cl^- concentration in the solution also increases. On the one hand, the electrolyte resistance decreases, the solution conductivity increases, and therefore Cl^- is easier to reach the metal surface. The Cl^- destroys the dynamic equilibrium state of dissolution and repair (repassivation) of the passivation film. Consequently, the dissolution is in the dominant position. This is because the Cl^- can preferentially and selectively adsorb on the passivation film and crowd out the oxygen atoms. The soluble chloride is formed by combining Cl^- with the cation of the passivation film. On the other hand, the polarization resistance decreases, and the I_{Corr} values of each alloy increases, thereby increasing the corrosion rate. As shown in Fig. 5b, the differences in I_{Corr} and R_p values among 2099-T83, 2060-T8, and 2A97-T6 alloys are increased. The corrosion resistance of 2060-T8 and 2099-T83 alloys is further weakened with increasing the Cl^- concentration, and that of 2A97-T6 alloy is still relatively fine. The I_{Corr} value and corrosion rate of the 2024-T4 alloy are still the highest, and the surface exhibits extensive exfoliation corrosion.

When the corrosion solution is 3.5wt% NaCl solution, which simulates the seawater environment, the corrosion morphologies and 3D surface morphologies of different alloys are shown in Fig. 6. The corrosion degree of all alloys is further aggravated with increasing the NaCl solution concentration, which declares that the increase in Cl^- concentration has a strong destructive effect on the oxide film on the alloy surface. Larger and deeper (43.86 μm) pits appear on the surface of 2A97-T3 alloy. The surface of 2A97-T6 alloy is mostly complete, but the number of pits is increasing. The pit depth is 49.45 μm. The 2060-T8 and 2099-T83 alloys

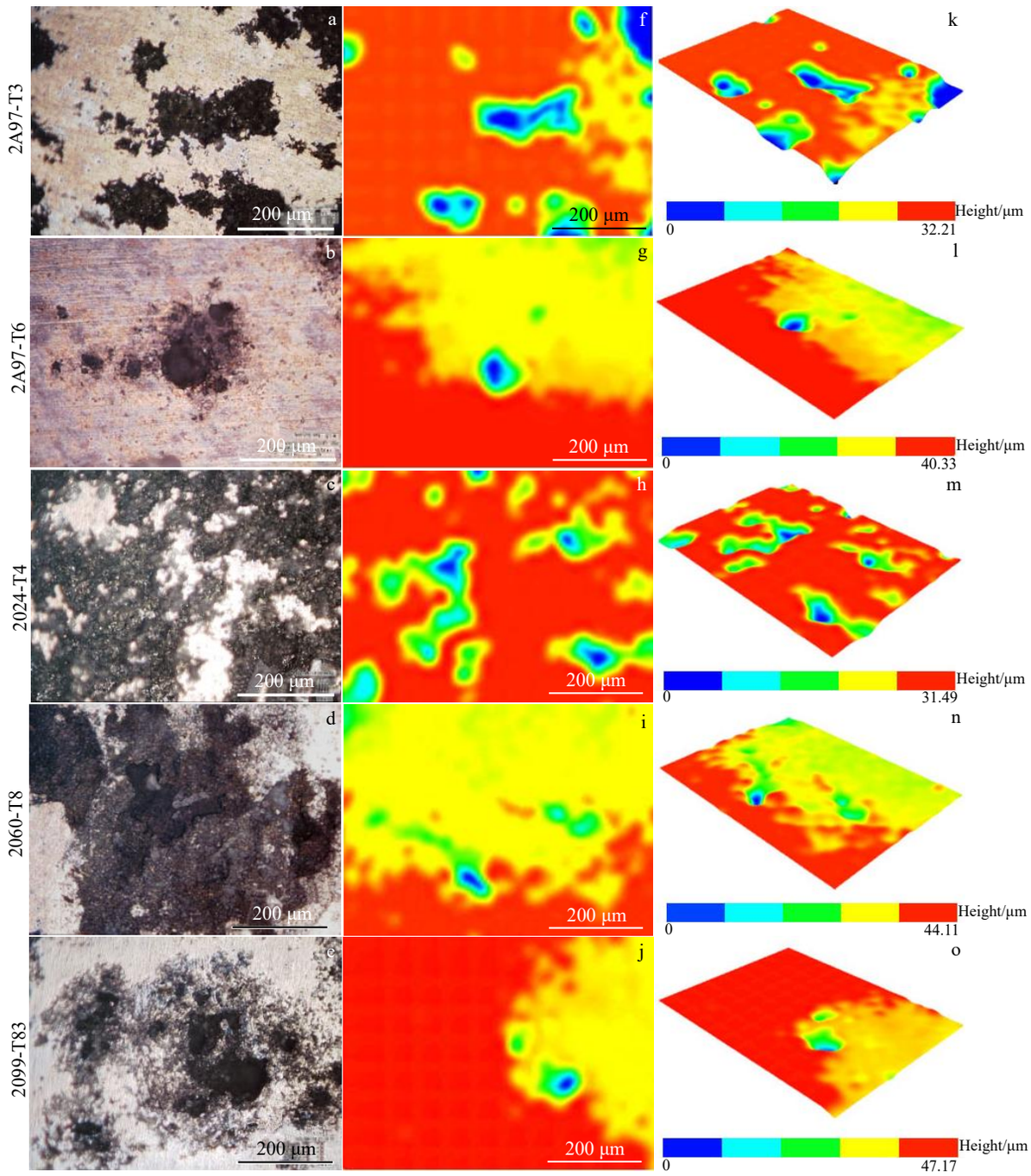

Fig.4 Corrosion morphologies (a–e), height distributions (f–j), and 3D surface morphologies (k–o) of 2A97-T3 (a, f, k), 2A97-T6 (b, g, l), 2024-T4 (c, h, m), 2060-T8 (d, i, n), and 2099-T83 (e, j, o) alloys after immersion in 2wt% NaCl solution

exhibit the most severe corrosion degree. Moreover, the pit depth of 2099-T83 alloy is the deepest of 60.46 μm. The passive film of the 2024-T4 Al alloy is rapidly broken. The external corrosion potential is excessively high, leading to the rapid fracture of passive film, which is the primary cause of the fast initial corrosion rate. Besides, obvious pitting corrosion occurs. However, the corrosion depth of 2024-T4 alloy is the shallowest of all alloys, which is only 39.56 μm. In conclusion, the corrosion resistance of 2A97-T3 alloy is still the best of all alloys in 3.5wt% NaCl solution.

The potentiodynamic polarization curves and electrochemical parameters of different alloys immersed in 5wt% NaCl solution are shown in Fig. 7. The order of E_{Corr} values of different alloys can be arranged as follows: 2A97-T3> 2A97-T6>2024-T4>2060-T8>2099-T83. This result is still consistent with that in Fig.3 and Fig.5, but the E_{Corr} difference between each alloy is further increased, compared with the results of alloys immersed in 2wt% and 3.5wt% NaCl solutions. The E_{Corr} value of 2A97-T3 alloy (−325.5 mV) is the largest and its fluctuation is the smallest, suggesting that the corrosion sensitivity of 2A97-T3 alloy is still the lowest, i.e., the 2A97-T3 alloy can hardly be corroded. The 2099-T83

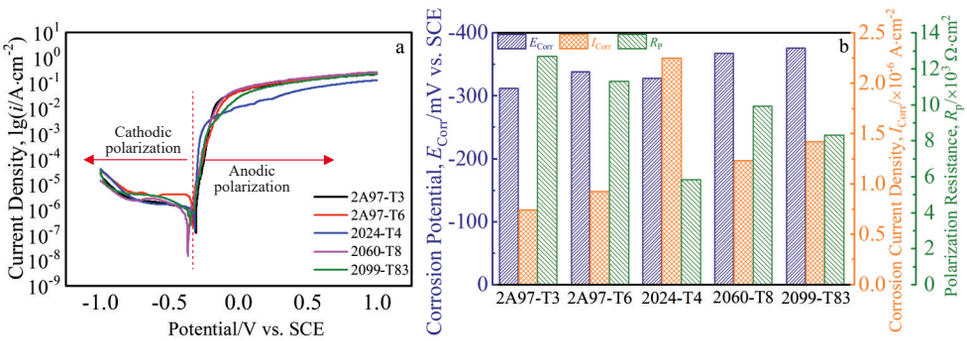

Fig.5 Potentiodynamic polarization curves (a) and electrochemical parameters (b) of different alloys immersed in 3.5wt% NaCl solution

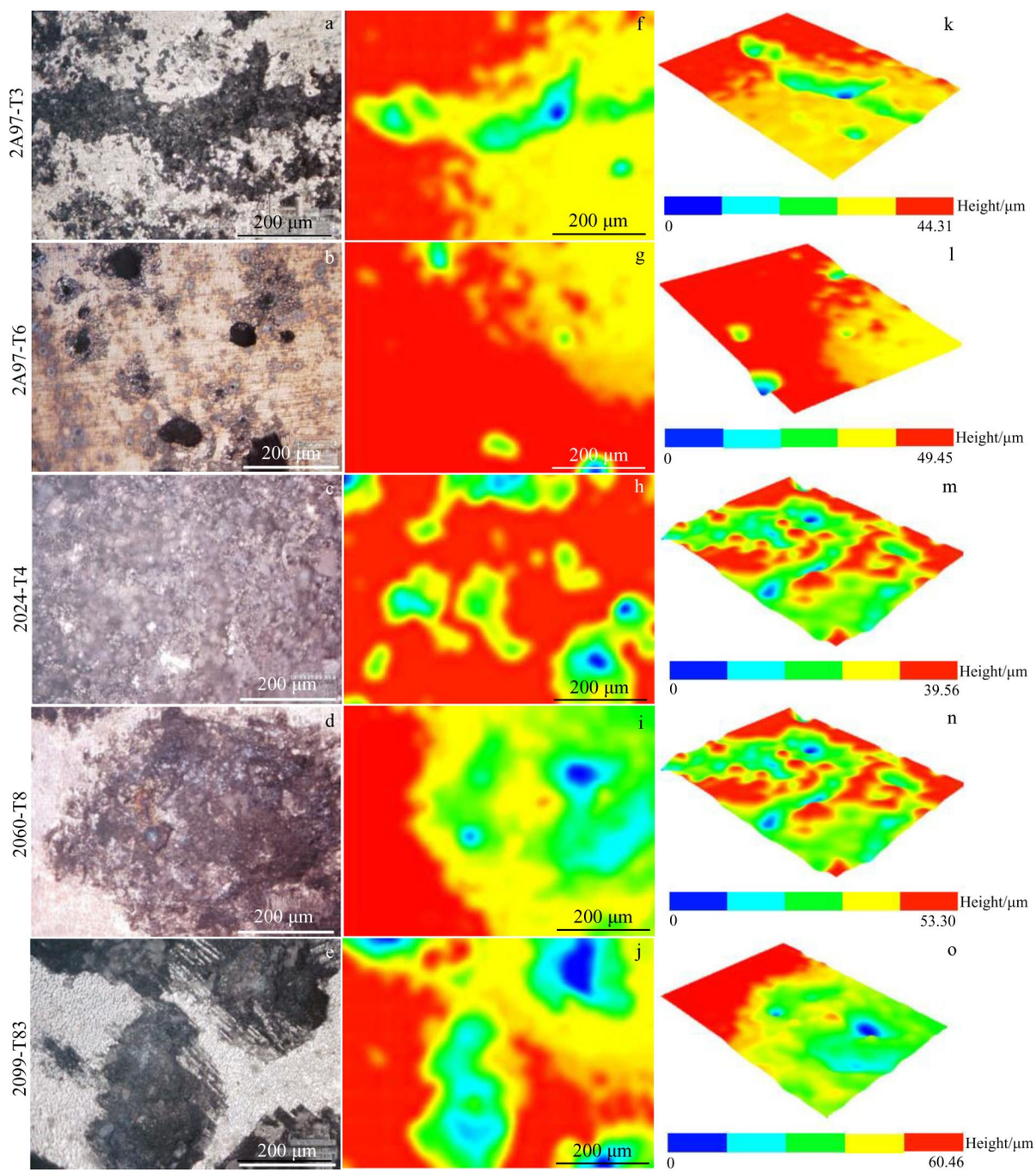

Fig.6 Corrosion morphologies (a–e), height distributions (f–j), and 3D surface morphologies (k–o) of 2A97-T3 (a, f, k), 2A97-T6 (b, g, l), 2024-T4 (c, h, m), 2060-T8 (d, i, n), and 2099-T83 (e, j, o) alloys after immersion in 3.5wt% NaCl solution

alloy has the lowest E_{Corr} value (−410.5 mV). Therefore, the 2099-T83 alloy has the highest corrosion sensitivity. Besides, the 2A97-T6 alloy has higher corrosion susceptibility than the 2A97-T3 alloy does.

When the NaCl solution concentration increases from 3.5wt% to 5wt%, the I_{Corr} of each alloy further increases and the polarization resistance decreases, resulting in the further increase in the corrosion rate. According to Fig.7b, the 2A97-T3 alloy still has the optimal corrosion resistance. The difference in I_{Corr} and R_p values among the 2A97-T6, 2060-T8, and 2099-T83 alloys further expands, which proclaims that the corrosion resistance of the 2060-T8 and 2099-T83 alloys is degraded with increasing the Cl^- concentration. Moreover, the I_{Corr} and the corrosion rate of 2024-T4 alloy are still the largest and its surface is completely corroded.

The local dissolution is promoted by the competitive adsorption of Cl^- and oxygen on the specimen surface. Furthermore, the chloride ions and cations combine to form soluble chloride due to the strong bonding between Cl^- and cations in the passivation film. The formed soluble chloride accumulates at some specific points on the newly exposed substrate surface, and some small pits also appear. The small pits are formed due to the adsorption of Cl^- ions. The higher the Cl^- concentration, the more the Cl^- adsorption. In addition, the more the cations for bonding, the more the newly formed small pits.

When the corrosion solution is 5wt% NaCl solution, the corrosion morphologies and 3D surface morphologies of different alloys are shown in Fig.8. The pits of 2A97-T3 alloy become larger and deeper, even encroaching on each other. The corrosion degree of 2A97-T3 and 2A97-T6 alloys is more severe, and their pit depth is also increasing. The corrosion of 2060-T8 and 2099-T83 alloys is the most serious. Furthermore, the surface of 2060-T8 and 2099-T83 alloys peels off, and the newly exposed area is subsequently corroded. The surface of 2024-T4 alloy is completely peeled off, so the matrix has some pits.

The schematic diagram of the electrochemical corrosion behavior of Al alloy in NaCl solution is shown in Fig.9. The occurrence of pitting in Al alloy is closely related to the active anions (especially Cl^-) in the corrosive medium. When the Al alloy is immersed in the Cl^--containing solution, the Cl^- and O_2 competitively adsorb on the oxide film, or the Cl^- firstly adsorbs on the active sites of the Al matrix. Subsequently, the chemical reaction of the Cl^- with the metal cations occurs in the oxide film, which reduces the oxide film and dissolves the Al matrix. Then, the thinned area on the oxide film is destroyed at a certain anode potential. Additionally, the catalytic process is promoted, since the metal cations form the chloride ion complexes rather than the hydrated oxide ions at the electrode interface. The dissolution rate of the local oxide film increases dramatically as the oxide film is disrupted, which leads to the formation of corrosion pits.

With increasing the polarization potential, the exposed Al matrix is dissolved and the pits are formed. Then, the oxygen absorption reaction of the cathode occurs on the outer surface of the etched hole. A gradient of electrical potential appears, owing to the continuously increasing metal ions in the pits, which causes the electromigration of aggressive anions into the pits. Meanwhile, the hydrolysis of Al^{3+} occurs. The abovementioned reactions can be expressed by Eq.(1−3), as follows:

$$Al - 3e^- \rightarrow Al^{3+} \quad (1)$$

$$O_2 + 2H_2O + 4e^- \rightarrow 4OH^- \quad (2)$$

$$Al^{3+} + H_2O + Cl^- \rightarrow H^+ + AlOHCl^+ \quad (3)$$

As a result, the hydrogen ion concentration of the solution increases in the pits, and therefore the solution is acidified. In other words, the corrosive medium changes from NaCl solution into HCl solution in the pits, which causes the Al matrix at the active dissolution state. Furthermore, the dissolution of the Al matrix is promoted, due to the hydrogen ions generated by hydrolysis and the Cl^- ions in the pits. The self-catalytic reaction of the Al matrix occurs, as expressed by Eq.(4), as follows:

$$Al + 3H^+ + 2Cl^- \rightarrow \frac{3}{2}H_2 + AlCl_2^+ \quad (4)$$

The repassivation of the Al matrix is hindered in the pits by two factors. One is that the concentrated NaCl solution possesses a high conductivity in the pits, so the resistance of the occluded cell becomes low, and the dissolution of Al matrix proceeds continuously. The other is that the oxygen solubility is very low in the concentrated NaCl solution. Thus, the oxygen can hardly diffuse into the pits. In addition, the corrosion reaction is also hindered to a certain extent in the pits by the corrosion products formed around the pits. When the corrosion products completely cover the pits, the diffusion

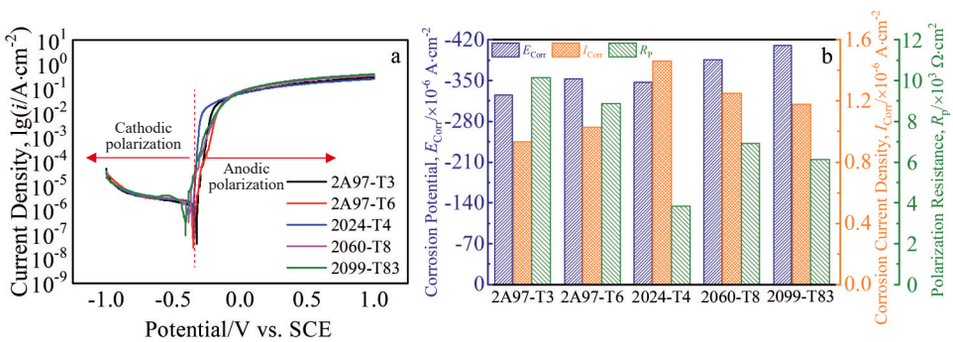

Fig.7 Potentiodynamic polarization curves (a) and electrochemical parameters (b) of different alloys immersed in 5wt% NaCl solution

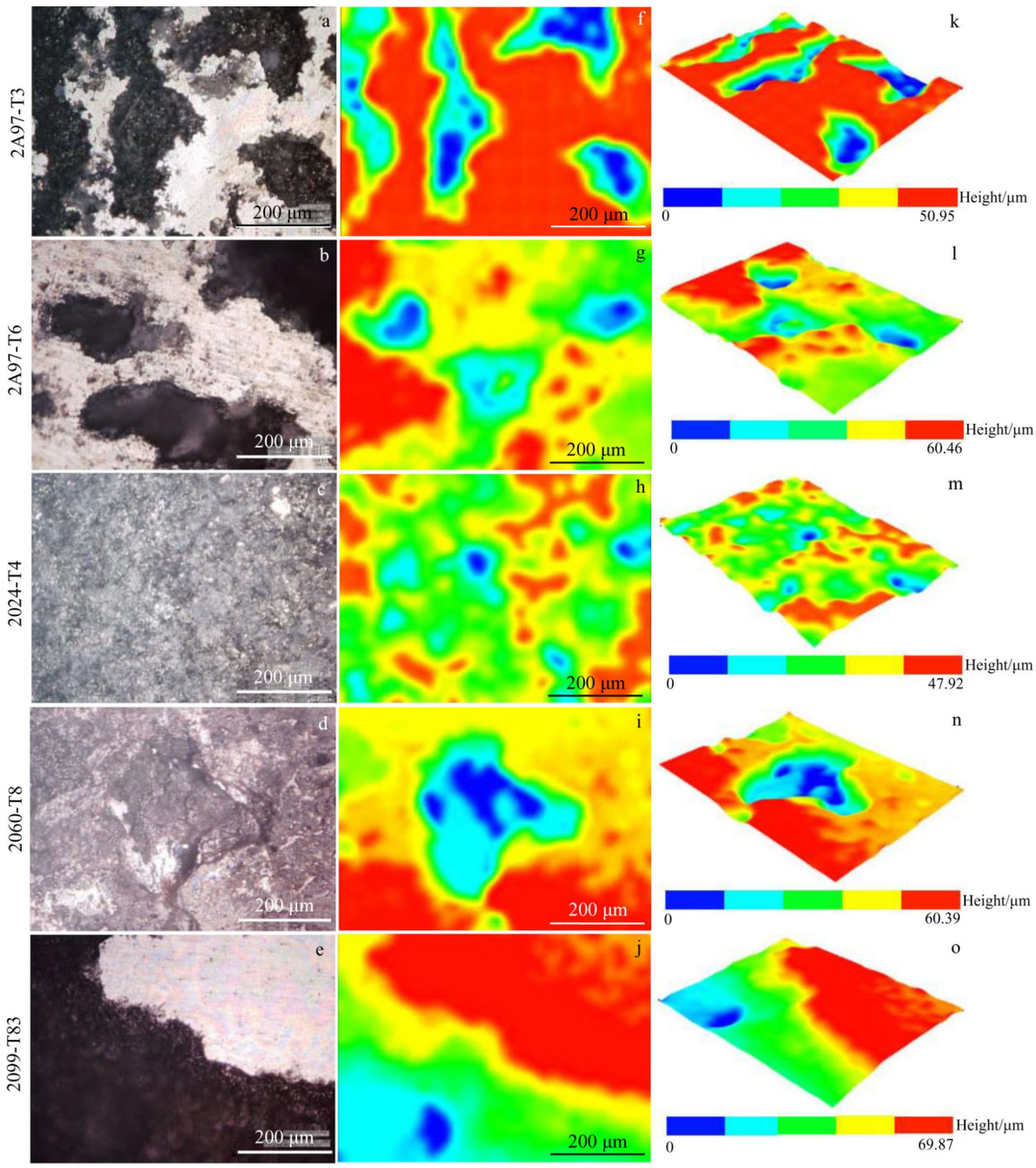

Fig.8 Corrosion morphologies (a–e), height distributions (f–j), and 3D surface morphologies (k–o) of 2A97-T3 (a, f, k), 2A97-T6 (b, g, l), 2024-T4 (c, h, m), 2060-T8 (d, i, n), and 2099-T83 (e, j, o) alloys after immersion in 5wt% NaCl solution

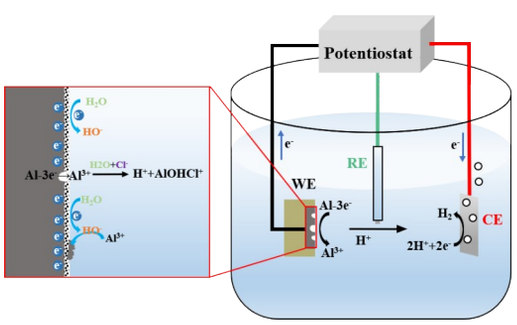

Fig.9 Schematic diagram of corrosion polarization behavior of Al alloy in NaCl solution

and convection of ions are blocked. Finally, the growth of pits is gradually inhibited.

3 Conclusions

1) The corrosion resistance of different Al alloys in NaCl solution can be arranged in order, as follows: 2A97-T3>2A97-T6>2024-T4>2060-T8>2099-T83.

2) The Cl^- destroys the dynamic equilibrium state of dissolution and repassivation of the passivation film, resulting in the dominant position of dissolution. The Cl^- interacts with cations to form soluble chlorides, which causes the pits on the alloy surface. The higher the Cl^- concentration, the more the

soluble chlorides, and the more the pits on the alloy surface.

3) The main strengthening precipitates of 2A97-T6 alloy are the T_1, θ, and δ' phases. The T_1 phase increases significantly with a more uniform distribution after the solid solution processing coupled with double-stage artificial aging. The phase size does not change significantly.

4) The exfoliation corrosion morphology of 2A97-T3 alloy is caused by the dissolution of intergranular θ phase. The pitting morphology of 2A97-T6 alloy is caused by the dissolution of intragranular T_1 phase.

5) In the corrosion solution, the T_1 phase of 2A97-T3 and 2A97-T6 alloys acts as the anode, and the matrix around the T_1 phase acts as the cathode, forming the primary battery. Thus, the anodic dissolution of the T_1 phase occurs. The T_1 phase reduces the potential difference between grain boundary and grain. Thus, the driving force of intergranular corrosion is reduced. Therefore, the intergranular corrosion is transformed into intragranular corrosion.

References

1 El-Aty A A, Xu Y, Guo X Z *et al. Journal of Advanced Research* [J], 2018, 10: 49

2 El-Aty A A, Xu Y, Zhang S H *et al. Procedia Engineering*[J], 2017, 207: 13

3 Paz Martínez-Viademonte M, Abrahami S T, Hack T *et al. Coatings*[J], 2020, 10(11): 1011

4 Fu B L, Qin G L, Meng X M *et al. Materials Science and Engineering A*[J], 2014, 617: 1

5 Peng Haoyun, Xie Hongzhi, Bai Xueshan *et al. Rare Metal Materials and Engineering*[J], 2021, 50(4): 1398 (in Chinese)

6 Ioja R J, Liu J. *Metallurgical & Materials Transactions A*[J], 2012, 43(9): 3325

7 Khokhlatova L B, Kolobnev N I, Oglodkov M S *et al. Metallurgist*[J], 2012, 56: 336

8 Tolga D, Costas S. *Materials & Design*[J], 2014, 56: 862

9 Wanhill R J H, Bray G H. *Aerostructural Design and Its Application to Aluminum-Lithium Alloys*[M]. Oxford: Butterworth-Heinemann, 2014

10 Zhang P, Chen M H, Chen W *et al. Microscopy Research and Technique*[J], 2021, 84(2): 358

11 Yu Juan, Lu Zheng, Lu Yuan *et al. Journal of Materials Engineering*[J], 2021, 49(5): 130 (in Chinese)

12 Lei X W, Nuam V L, Bai Y *et al. Journal of Alloys and Compounds*[J], 2021, 855(Part 2): 157 519

13 Zhang P, Chen M H. *Metal Science and Heat Treatment*[J], 2021, 63(1–2): 47

14 Liao Zhongquan, Zheng Ziqiao, Zhong Shen *et al. Powder Metallurgy Materials Science and Engineering*[J], 2011, 16(4): 478 (in Chinese)

15 Lin Y, Zheng Z Q, Zhang H F *et al. Transactions of Nonferrous Metals Society of China*[J], 2013, 23(6): 1728

16 Zhong J, Zhong S, Zheng Z Q *et al. Transactions of Nonferrous Metals Society of China*[J], 2014, 24(2): 303

17 Xue X L, Zheng Z Q, Hu F *et al. Rare Metal Materials and Engineering*[J], 2016, 45(12): 3319

18 Gao C, Luan Y, Yu J C *et al. Transactions of Nonferrous Metals Society of China*[J], 2014, 24(7): 2196

19 Zhang X X, Zhou X R, Hashimoto T *et al. Corrosion Science*[J], 2018, 132: 1

20 Luo C, Zhang X X, Zhou X R *et al. Journal of Materials Engineering and Performance*[J], 2016, 25: 1811

21 Chen B, Li C H, He S C *et al*. *Journal of Materials Research*[J], 2014, 29(12): 1344

22 Huang J L, Li J F, Liu D Y *et al. Corrosion Science*[J], 2018, 139: 215

23 Proton V, Alexis J, Andrieu E *et al. Corrosion Science*[J], 2014, 80: 494

24 Guyot P, Cottignies L. *Acta Materialia*[J], 1996, 44(10): 4161

25 Xu L Z, Tong C Y, Zhan L H *et al. Materials Science and Engineering A*[J], 2022, 851: 143 581

26 Kumai C, Kusinski J, Thomas G *et al. Corrosion*[J], 1989, 45(4): 294

27 Zhang X X, Zhou X R, Hashimoto T *et al. Corrosion Science*[J], 2017, 116: 14

28 Buchheit R G, Moran J P, Stoner G E. *Corrosion*[J], 1994, 50(2): 120

29 Zhang X X, Zhou X R, Hashimoto T *et al. Corrosion Science*[J], 2018, 135: 177

30 Luo C, Gao M, Sun Z *et al. Corrosion Engineering, Science and Technology*[J], 2015, 50(5): 390

31 Niu J T, Liu Z Q, Yang Q *et al*. *Materials and Corrosion*[J], 2022, 73(2): 171

32 Zhang P, Chen M H. *Journal of Materials Science*[J], 2020, 55: 9828

33 Osório W R, Freitas E S, Garcia A. *Electrochimica Acta*[J], 2013, 102: 436

34 Bononi M, Conte M, Giovanardi R *et al. Surface and Coatings Technology*[J], 2017, 325: 627

35 Kertz J E, Gouma P I, Buchheit R G. *Metallurgical and Materials Transactions A*[J], 2011, 32(10): 2561

36 Boguslaw M, Antoni P. *Corrosion Science*[J], 1983, 23(7): 697

37 Buchheit R G, Moran J P, Stoner G E. *Corrosion*[J], 2012, 46(8): 610

38 Li J F, Ye Z H, Liu D Y *et al. Acta Metallurgica Sinica*[J], 2017, 30: 133

39 Gable B M, Zhu A W, Csontos A A *et al. Light Metal*[J], 2001, 1(1): 1

40 Proton V, Alexis J, Andrieu E *et al. Corrosion Science*[J], 2014, 80: 494

41 Gao C, Luan Y, Yu J C *et al. Transactions of Nonferrous Metals Society of China*[J], 2014, 24(7): 2196

42 Li J F, Li C X, Peng Z W *et al. Journal of Alloys and Compounds*[J], 2008, 460(1–2): 688

43 Li J F, Zheng Z Q, Li S C *et al. Corrosion Science*[J], 2007, 49(6): 2436
44 Luo C, Albu S A, Zhou X R *et al. Journal of Alloys and Compounds*[J], 2016, 658: 61
45 Lei X W, Nuam V L, Yuan Y X *et al. Journal of Alloys and Compounds*[J], 2021, 873: 159 765
46 Cai Chao, Li Jinfeng, Wang Heng *et al. Rare Metal Materials and Engineering*[J], 2015, 44(10): 2523 (in Chinese)
47 Ghosh K S, Hilal M, Bose S. *Transactions of Nonferrous Metals Society of China*[J], 2013, 23(11): 3215
48 Younis A A, El-Sabbah M M B, Holze R. *Journal of Solid State Electrochemistry*[J], 2012, 16: 1033

人工时效和腐蚀介质浓度对2A97 Al-Cu-Li合金电化学腐蚀行为的影响

张　鹏，赵新生，饶思贤
(安徽工业大学 机械工程学院，安徽 马鞍山 243032)

摘　要：采用动电位极化曲线电化学方法研究了2A97-T3和2A97-T6 Al-Cu-Li合金的耐腐蚀性能，并以第3代典型2060-T8合金、2099-T83铝锂合金和航空用2024-T4高强铝合金为参考对象进行了比较。通过分析电化学参数和腐蚀形貌，发现合金在3种浓度的NaCl溶液中的耐腐蚀性为2A97-T3>2A97-T6>2024-T4>2060-T8>2099-T83。随着NaCl溶液浓度的增加，合金的腐蚀电位（E_{Corr}）均降低，同时加剧了表面点蚀和晶间腐蚀程度。2A97-T3合金通过进行固溶和双级人工时效处理的共同作用得到2A97-T6合金，此时T_1相数量大大增加且分布更加均匀。因此，热处理工艺降低了2A97铝合金的腐蚀电位，导致2A97-T6合金的耐腐蚀性能略弱于2A97-T3合金。晶间θ相的解体诱导了2A97-T3合金的剥落腐蚀形貌，而2A97-T6合金的点蚀形貌是由晶内T_1相的溶解造成的。

关键词：Al-Cu-Li合金；电化学极化；腐蚀电位；热处理；腐蚀形貌

作者简介：张　鹏，男，1989年生，博士，讲师，安徽工业大学机械工程学院，安徽 马鞍山 243032，E-mail：zhangpeng_105@ahut.edu.com